Focus Section: Intermountain West Earthquakes in Spring 2020

The 31 March 2020 M_w 6.5 Stanley, Idaho, Earthquake: Seismotectonics and Preliminary Aftershock Analysis

Lee M. Liberty*[1], Zachery M. Lifton[2], and T. Dylan Mikesell[1]

Abstract

We report on the tectonic framework, seismicity, and aftershock monitoring efforts related to the 31 March 2020 M_w 6.5 Stanley, Idaho, earthquake. The earthquake sequence has produced both strike-slip and dip-slip motion, with minimal surface displacement or damage. The earthquake occurred at the northern limits of the Sawtooth normal fault. This fault separates the Centennial tectonic belt, a zone of active seismicity within the Basin and Range Province, from the Idaho batholith to the west and Challis volcanic belt to the north and east. We show evidence for a potential kinematic link between the northeast-dipping Sawtooth fault and the southwest-dipping Lost River fault. These opposing faults have recorded four of the five M ≥ 6 Idaho earthquakes from the past 76 yr, including 1983 M_w 6.9 Borah Peak and the 1944 M 6.1 and 1945 M 6.0 Seafoam earthquakes. Geological and geophysical data point to possible fault boundary segments driven by pre-existing geologic structures. We suggest that the limits of both the Sawtooth and Lost River faults extend north beyond their mapped extent, are influenced by the relic trans-Challis fault system, and that seismicity within this region will likely continue for the coming years. Ongoing seismic monitoring efforts will lead to an improved understanding of ground shaking potential and active fault characteristics.

Cite this article as Liberty, L. M., Z. M. Lifton, and T. Dylan Mikesell (2020). The 31 March 2020 M_w 6.5 Stanley, Idaho, Earthquake: Seismotectonics and Preliminary Aftershock Analysis, *Seismol. Res. Lett.* **92**, 663–678, doi: 10.1785/0220200319.

Introduction

The rugged and remote mountains of central and eastern Idaho host a robust earthquake record. These earthquakes initiate along mostly north- to northwest-striking normal faults, with a clear surface expression that reflects the Quaternary earthquake record (Fig. 1). On Tuesday, 31 March 2020, at 5:52 p.m. local time (23:52 UTC), the Stanley, Idaho, earthquake of moment magnitude (M_w) 6.5 occurred near the intersection of the northwest-trending Sawtooth normal fault and the northeast-trending trans-Challis fault system (TCFS). The earthquake was the largest in Idaho, since the 1983 M_w 6.9 Borah Peak event (e.g., Crone *et al.*, 1987; Richins *et al.*, 1987). The epicenter (44.4603° N, 115.136° W) was about 30 km northwest of the mountain community of Stanley and within 15 km of both the 1944 **M** 6.1 and 1945 **M** 6.0 Seafoam earthquakes (Dewey, 1987). Although, the Stanley earthquake may have initiated along the Sawtooth normal fault, the lack of a surface rupture, coupled with observed mainshock and preliminary aftershock characteristics, suggest a complex interplay between both a known active fault and unknown faults with no surface expression. Although, the Stanley earthquake caused little damage due its remote central Idaho location, its seismological characteristics are relevant to active fault systems throughout the intermountain west.

The M_w 6.5 Stanley earthquake was felt throughout the U.S. Pacific Northwest, but only minor structural damage was identified due to its remote location. In the epicentral area, a modified Mercalli intensity of 7.5 was assessed from reports of damage by residents. Overflights in the epicentral area revealed extensive snow avalanches and rockfall, which, in some cases, blocked roads and temporarily dammed rivers. Three prominent rock spires that hosted popular climbing routes toppled during mainshock or aftershock shaking. In addition, at least one case of liquefaction and lateral spread was documented at Stanley Lake (Fig. 2), where unconsolidated delta sediments and shoreline deposits collapsed into the lake. Many sand boils and tension cracks were observed and documented along the northwest shore of the lake (Idaho Geological Survey, 2020). In the resort community of Sun Valley (~100 km epicentral distance) and the capital city of Boise (~115 km epicentral distance), modified Mercalli intensities of 4 were reported.

1. Department of Geosciences, Boise State University, Boise, Idaho, U.S.A.; 2. Idaho Geological Survey, Idaho Water Center, Boise, Idaho, U.S.A.

*Corresponding author: lliberty@boisestate.edu

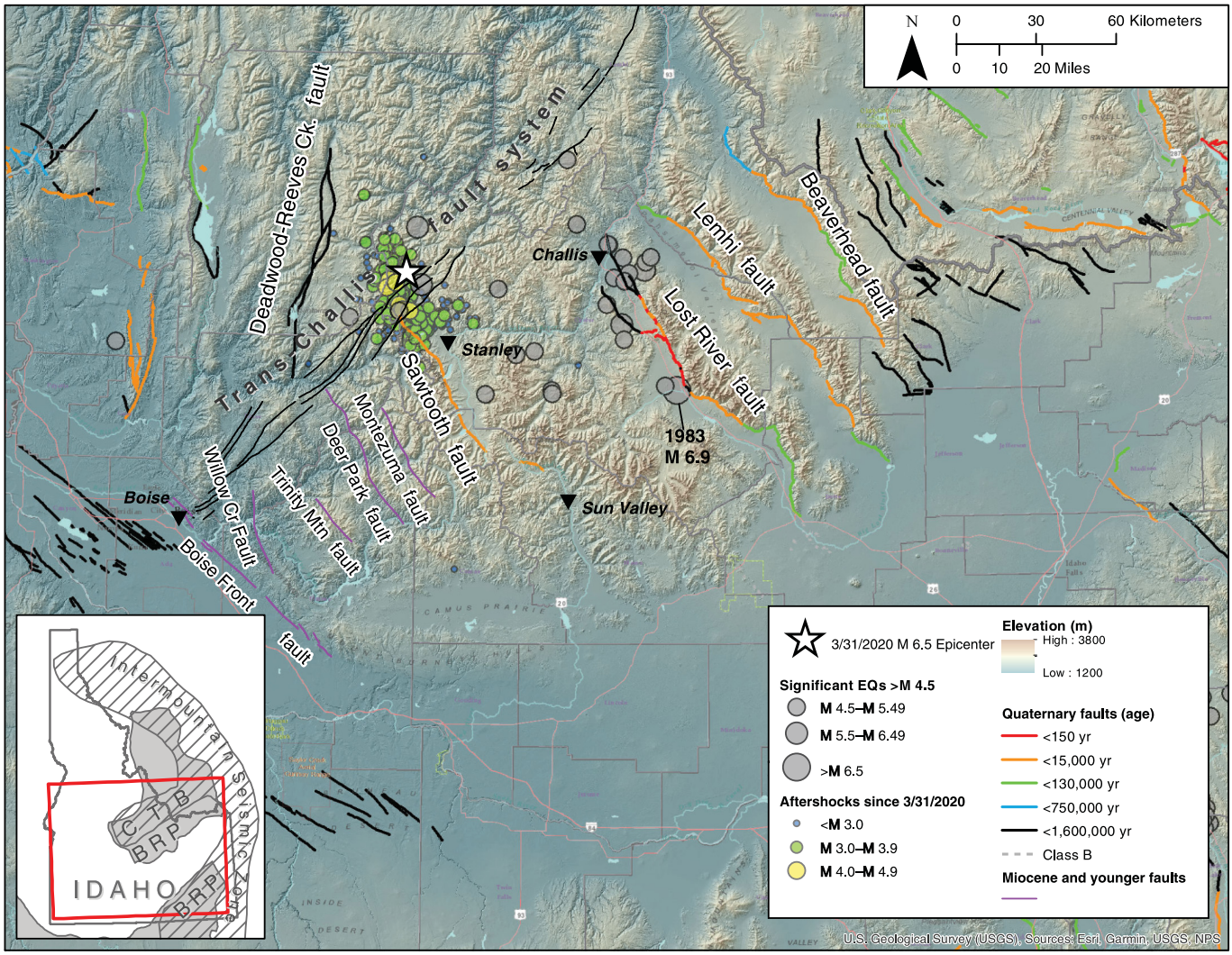

In this article, we report on the M_w 6.5 Stanley earthquake, the geological and geophysical framework for central Idaho, the history of regional seismicity, and a four-month aftershock synopsis. We compare temporal and spatial aftershock characteristics with the aftershock sequence related to 1983 Borah Peak earthquake that initiated along the parallel Lost River fault system (Fig. 1) and also with other regional and relevant earthquakes. With the aid of existing geophysical datasets, we explore geologic relationships to previously proposed fault segment boundaries, and offer a potential kinematic link between the Sawtooth and Lost River faults. Finally, we discuss our rapidly deployed temporary seismic monitoring network that will improve our understanding of the earthquake aftershock characteristics and fault geometries.

31 March 2020 M_w 6.5 Stanley Earthquake

Initial field reconnaissance of the epicentral area was hindered by several factors, including heavy late March snowfall and travel restrictions related to the COVID-19 pandemic.

Figure 1. Regional topographic relief map of southern Idaho with recorded earthquakes **M** > 4.5 and aftershocks from the M_w 6.5 Stanley earthquake. Quaternary-active faults are from the Quaternary Fold and Fault Database (U.S. Geological Survey and Idaho Geological Survey, 2020), Miocene and younger faults are from Breckenridge *et al.* (2003), and the trans-Challis fault system (TCFS) is from Lewis *et al.* (2012). Inset map shows extent of Basin and Range Province (BRP; gray shading), Centennial tectonic belt (CTB), and Intermountain seismic zone (diagonal lines) in and around Idaho. Aftershocks and historical seismicity are from the U.S. Geological Survey (USGS) comprehensive earthquake catalog (U.S. Geological Survey, 2020b).

Whereas these restrictions limited early field reconnaissance, remote sensing data suggest that this earthquake did not produce discrete ground surface rupture. A summer field visit reinforced this earlier observation of no earthquake-related surface deformation. While not unusual for an M_w 6.5 earthquake, surface displacements closer to 0.5 m may be expected (Wells and Coppersmith, 1994).

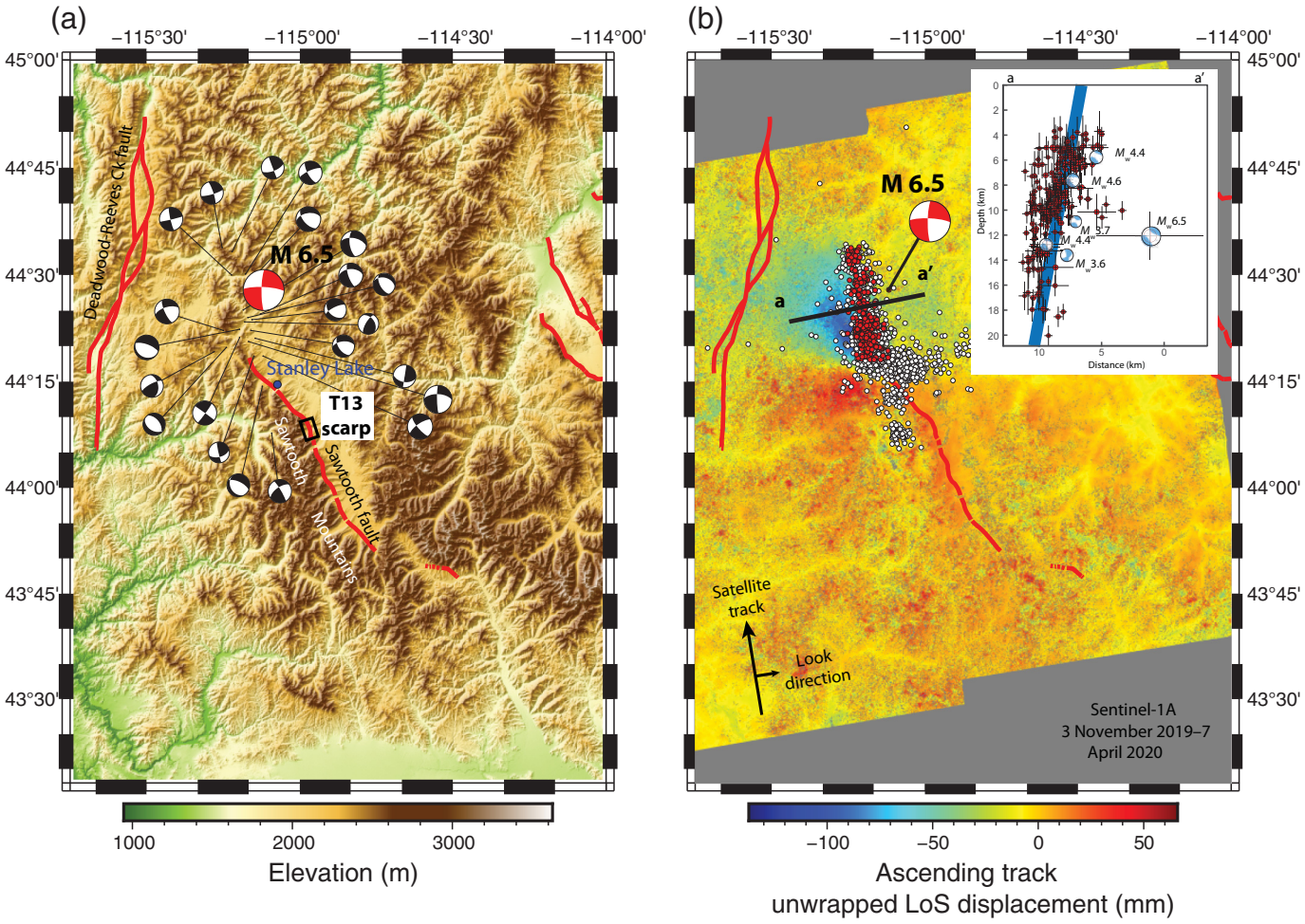

Figure 2. (a) Topographic relief map of the Sawtooth fault region. Mainshock focal mechanism is from the Global Centroid Moment Tensor catalog (Dziewonski *et al.*, 1981; Ekström *et al.*, 2012); aftershock focal mechanisms are from the International Seismological Centre (2020). (b) Unwrapped line-of-sight (LoS) displacement Interferometric Synthetic Aperture Radar interferogram of the 31 March 2020 M_W 6.5 Stanley earthquake. Interferogram was created from Sentinel-1 ascending track data acquired 3 November 2019 and 7 April 2020. Red lines are faults from the U.S. Geological Survey and Idaho Geological Survey (2020). Red circles on (b) represent aftershocks within the northern epicentral region with depth uncertainties of less than 4 km. White circles represent all other pre-31 July 2020 aftershocks. Inset figure on (b) shows aftershocks, in cross section, for the northern epicentral region. Black lines represent horizontal and vertical uncertainty estimates, and thick blue line represents a 70° west-dipping fault that best fits the aftershock locations. Only earthquakes highlighted as red circles on (b) are included in the cross section. Maps were created with Generic Mapping Tools (Wessel and Smith 1998) and Generic Mapping Tools Synthetic Aperture Radar (Sandwell *et al.*, 2011).

Interferometric Synthetic Aperture Radar data, processed from a pair of Sentinel-1A ascending track radar images from 3 November 2019 and 7 April 2020, identify a broad but modest region of deformation. This preliminary analysis suggests no discrete surface rupture and only about 0.1 m of surface deformation over about 10 km^2 (Fig. 2b). Here, line-of-sight displacements show down to the west motion (Fig. 2b). This contradicts the long-term motion along the down-to-the-east Sawtooth fault that is mapped within the aftershock region.

Motion from the Stanley earthquake and aftershocks is enigmatic, and does not resemble a typical normal-faulting event of the region (e.g., Doser and Smith, 1989). The earthquake was recorded at a depth of 14.5 ± 3 km, with a preferred north–south fault-plane solution. Moment tensor solutions for the mainshock and aftershocks suggest a mix of strike-slip and dip-slip fault motion. A slight rotation in the alignment of the northern aftershock region is consistent with left-lateral strike-slip motion, to account for a complex fault geometry. Finite-fault modeling using the north-northwest-striking (352° azimuth, dipping 74° to the east) left-lateral nodal-plane focal mechanism solution are consistent with this observation (U.S. Geological Survey, 2020a). These results suggest that the fault ruptured to a minimum depth of 1 km, but did not reach the ground surface. In contrast to the negligible ground displacements that have been identified with the Stanley earthquake,

the 1983 M_w 6.9 Borah Peak earthquake produced mostly dip-slip motion along the range-bounding Lost River fault, with a maximum vertical displacement of 2.7 m (Fig. 1).

The earthquake epicenter was located a few kilometers to the north of the Sawtooth normal fault (Fig. 1), and many of the recorded aftershocks lie along this fault. Whereas the Sawtooth fault is mapped as a northeast-dipping normal fault, the north-striking nodal plane of the moment tensor solutions suggest a steep west-dipping fault plane. Although, not particularly well constrained because of the sparse regional seismic network, the presented aftershock sequence (31 March through 31 July 2020) outlines a ~50 km long zone, with the northern aftershocks trending roughly N10°W and the southern aftershocks trending roughly N20° W (Fig. 2).

When we examine the northern aftershocks with depth uncertainties of less than 4 km, and affiliated moment tensor solutions from the northern aftershock region, we see a steep west-dipping fault plane with a strong left-lateral strike-slip component (Fig. 2). Though opposite the expected direction of dip of the Sawtooth fault, this afterslip pattern is consistent with the two other large normal-faulting earthquakes of Idaho that were recorded with a modern seismic network. For both the 2014–2017 Challis, Idaho, sequence and the 2017 Sulphur Peak earthquake near Soda Springs, Idaho, aftershocks aligned along an opposite direction of fault dip, when compared with presumed fault geometries. For the Challis event, aftershocks outlined a steep east-dipping structure associated with a conjugate zone or fault network within the northern limits of the west-dipping Lost River fault (Pang *et al.*, 2018). For the Sulphur Peak earthquake, the best-fit for many of the aftershocks outlined a steep east-dipping fault plane related to the northern limits of the west-dipping eastern Bear Lake fault (Koper *et al.*, 2018; Pollitz *et al.*, 2019). While Pollitz *et al.* (2019) suggested that the anomalous aftershock patterns may be related to the reactivation of ancient thrust belt structures; this is likely not the case for the Stanley earthquake, where mostly Cretaceous granitic and Eocene volcanic rocks are mapped (Fig. 3). The common link between all three earthquake sequences is that they all initiated along the northern limits of their respective normal faults.

The southern aftershocks related to the Stanley earthquake have been recorded within 10 km of a Holocene-active down-to-the-east Sawtooth fault scarp (Thackray *et al.*, 2013; Fig. 2), but this band of seismicity lies almost entirely beneath the footwall side of the mapped Sawtooth fault. When we combine our observations of both the northern and southern aftershock regions, our preliminary aftershock assessment is that afterslip remains mostly within the granitic footwall, and not along the east-dipping Sawtooth fault. One exception to this observation is that a small cluster of relatively small magnitude aftershocks forms a N60°E-trending alignment to the north of Stanley. Here, no active faults are mapped, but this trend is consistent with motion along the ancient TCFS. There are few moment tensor solutions for aftershocks associated with this structure, due to the sparse regional monitoring network. An improved understanding of the aftershock sequence may become clearer, after data analysis from the temporary monitoring network is completed.

Geological Framework

Though it is unclear whether mainshock or aftershock motion can be considered as along the Sawtooth fault, aftershock alignment and proximity to this fault makes us believe that there is some interplay. The Sawtooth fault is one of four actively extending normal faults in central Idaho. This region of extension lies to the north of the Snake River Plain (SRP) and is a part of the Basin and Range Province (Fig. 1). Locally, this province is termed the Centennial tectonic belt (CTB) and consists of a series of subparallel, northwest-striking normal faults that contain Precambrian and Paleozoic sedimentary and metamorphic rocks within the ranges, and Neogene and younger sediments within the adjacent basins (Figs. 1 and 3; Stickney and Bartholomew, 1987). Three primary normal faults of the region are the Lost River, Lemhi, and Beaverhead (Fig. 1), which initiated about 16 Ma (Rodgers *et al.*, 2002). These 141 to 151 km long, subparallel, continuous, down-to-the-southwest faults accommodate significant vertical displacement of the crust, and each have clear geomorphic expressions along six well-defined segments (Crone and Haller, 1991). Vertical slip-rate estimates on the central portion of these faults range from between 0.2 and 0.7 mm/yr (Scott *et al.*, 1985; Haller and Wheeler, 2010). Based on paleoseismic and geomorphic indicators, Scott *et al.* (1985) suggested that the central segments of these three faults have experienced more Quaternary activity, when compared with the estimated slip of <0.2 mm/yr for the southern and northern segments.

The fourth major fault in the region is the down-to-the-northeast, 60 km long active Sawtooth normal fault, which also accommodates significant vertical displacement and forms a dramatic high-relief range front on the northeast side of the Sawtooth Mountains (Fig. 2). Extensive Pleistocene alpine glacial deposits extend across the fault and onto the valley floor. The Sawtooth Mountains, which consist mostly of Cretaceous granitic rocks of the Idaho batholith, produce about 1300 m of relief across the fault, with an uplifted horst block that hosts 57 peaks higher than 3000 m above sea level.

Umpleby and Livingston (1920) first recognized that the Stanley basin was likely a fault-bound structure. Early mapping in the area was done by Reid (1963), Kiilsgaard *et al.* (1970), Rember and Bennett (1979), Fisher *et al.* (1983), and Tschanz *et al.* (1986). Geomatrix Consultants, Inc. (1989) documented geomorphic evidence of Quaternary faulting, including deformed moraine crests. On the hanging wall, Tertiary and Quaternary sediments fill the Stanley basin (Tschanz *et al.*, 1986). While limited, gravity data outline a sedimentary basin

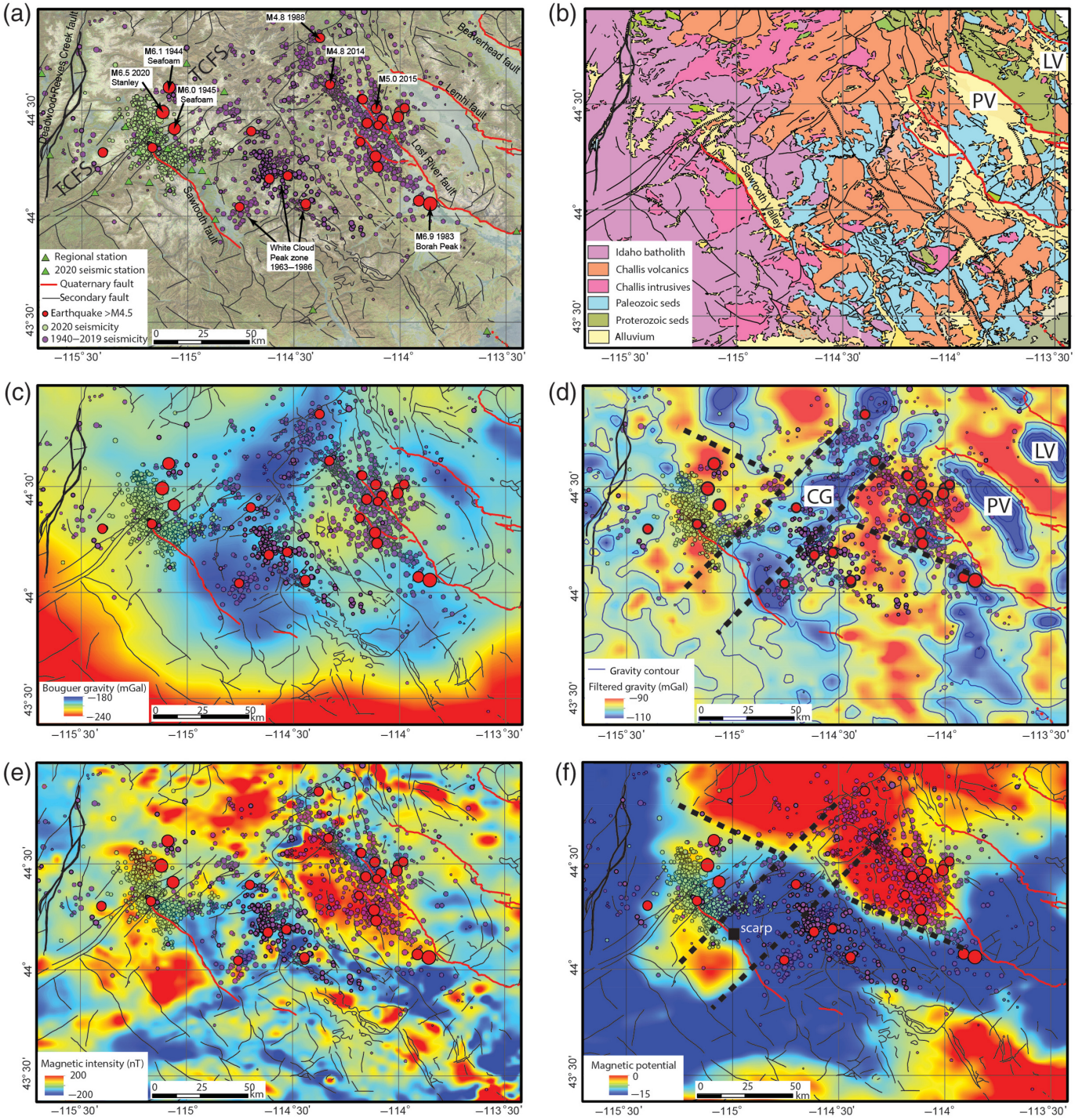

Figure 3. (a) Topographic and earthquake location map for east-central Idaho. Notable earthquakes discussed in the Historical and Modern Seismicity of Central Idaho section are labeled. (b) Simplified geologic map, modified from Lewis *et al.* (2012). (c) Complete Bouguer gravity anomaly map. (d) Bouguer gravity map of (c), filtered at 100 km to remove long spatial wavelengths. (e) Magnetic intensity. (f) Pseudogravity or magnetic potential map derived from (e). Each plot shows seismicity since 1944 (see Data and Resources) and mapped faults (U.S. Geological Survey and Idaho Geological Survey, 2020). Background seismicity (purple circles) and earthquakes **M** > 4.5 (red circles) are scaled by magnitude (National Earthquake Information Center catalog). Stanley aftershocks are shown as green circles. Dashed lines on (d,f) represent large horizontal gradients that reflect relic geologic structures. CG, Custer graben; LV, Lemhi Valley; PV, Pahsimeroi Valley.

that lies above the Sawtooth fault, with a focused depocenter adjacent to the southern reaches of the fault (Mankinen *et al.*, 2004; Thackray *et al.*, 2013; Fig. 3).

The timing of paleoearthquake Sawtooth fault surface rupture has been investigated but is not well understood, because a comprehensive paleoseismic study has yet been conducted. Thackray *et al.* (2013) used limited light detection and ranging topographic data, aerial photographs, and field mapping to document 4–9-meter-high scarps displacing 11–14 ka glacial deposits, and 2–3-meter-high scarps in Holocene alluvial deposits. From these observations, they interpreted two or three postglacial surface-rupturing events. Based on geomorphic expressions, they suggest two discrete fault segments. Thackray *et al.* (2013) estimated a Holocene slip rate of 0.5–0.9 mm/yr, higher than the long-term Quaternary slip rate estimate of <0.2 mm/yr (Crone *et al.*, 2010). Based on length–magnitude scaling relationships (Wells and Coppersmith, 1994) and the 2–3 m displacement, if related to a single surface-rupturing event, this suggests that this portion of the fault may have moved with similar moment release as the Borah Peak earthquake. If so, the entire length of the Sawtooth fault may have ruptured during one or more Holocene earthquake.

The northern mapped extent of the Sawtooth fault terminates near its intersection with the northeast-striking TCFS, a 24 km wide zone of normal faults that accommodated Eocene northwest–southeast extension (Fig. 1). Early extension was directly related to the emplacement of Challis volcanic rocks that lie to the north and east (Bennett, 1986; Payne *et al.*, 2012). The TCFS extends across Montana as the Great Falls lineament to form a regionally extensive structure (O'Neill and Lopez, 1985). The TCFS is not considered Quaternary-active, but its relationship to the adjacent and actively extending Basin and Range Province, and historic seismicity that appears along its mapped extent, suggests it may play a role in limiting the northern extent of fault motion. Although, moment tensor solutions from the Stanley earthquake suggest possible right-lateral strike-slip motion striking similar to the TCFS, there is no reported evidence of shear along the TCFS.

To the southeast of the TCFS, Kiilsgaard *et al.* (1986) mapped the 30 km wide Custer graben as a synvolcanic basin that accommodated Eocene extension and subsidence. This graben extends southwest to the Sawtooth fault and north to the town of Challis and the epicentral region of the 2014 **M** 4.8 Challis earthquake (Figs. 1 and 3). The graben can be best identified as a gravity low that is bound to the northwest by the TCFS and a parallel lineament to the southeast (Fig. 3). Although there is no direct evidence for active motion on faults that lie within this graben, the southern limit of the Stanley earthquake aftershocks, the N60°E alignment of some Stanley earthquake aftershocks, and the northern limit of the 2014–2017 Challis earthquake sequence (Pang *et al.*, 2018) all lie at the northern graben boundary. This may provide evidence that the graben has restricted earthquake ruptures, acts as a fault segment boundary, and is seismically active.

Although the Sawtooth fault has been recognized as the western limit of the CTB, Bennett (1986) mapped several subparallel northwest-striking faults to the southwest of the Sawtooth fault. This includes the Montezuma, Deer Park, Trinity Mountain, Willow Creek, and Boise Front faults (Fig. 1). These faults all may represent Basin and Range-style faults that accommodate much lower extension rates, compared with faults within the CTB. Although, these faults have been identified, no detailed fault mapping has been completed, and there are no clear geomorphic expressions supporting recent fault displacements. The northern ends of the northwest-trending subparallel faults, Sawtooth fault, and three faults within the CTB, all terminate at the TCFS (Bennett, 1986). Given the regional extent of the TCFS and related Great Falls lineament, and the termination of northwest-striking normal faults along this fault system, we suggest that these relic structures play a key kinematic role in active faulting both in Idaho and Montana.

Historical and Modern Seismicity of Central Idaho

Much of the regional historic seismicity has been focused on the northern limits of the Lost River and Sawtooth faults (Fig. 1). Temporal and spatial patterns of seismicity in eastern and central Idaho have been linked to a parabolic earthquake distribution that is responding to the thermal effect of the migrating Yellowstone hot spot (Anders *et al.*, 1989; Pierce and Morgan, 1992). The westward limit of the northern parabola arm aligns with the Sawtooth fault (Anders *et al.*, 1989, 2014), which lies approximately 85 km to the west of the Lost River fault (Fig. 1). Within the CTB, topographic relief suggests that the central portion of each fault has hosted the greatest cumulative moment release, yet much of the historic seismicity (**M** ≥ 4.5) is located along the northern portions of the Lost River and Sawtooth faults near the TCFS. Although, there is little evidence for historic seismicity along the Beaverhead and Lemhi faults, or along the southern segments of the Sawtooth and Lost River faults, similar relief and evidence for Holocene fault motion suggests that each fault segment is capable of hosting large earthquakes.

The earliest recorded seismicity for central Idaho has been termed the Seafoam sequence by Dewey (1987) and included two felt earthquakes. On 12 July 1944, an **M** 6.1 earthquake occurred and was located approximately 8 km to the southeast of the 2020 Stanley earthquake epicenter (Fig. 1). Seven months later, on 14 February 1945, an **M** 6.0 earthquake was recorded in the same region (Fig. 1). Although the epicentral locations were not well determined for this earthquake sequence (about ±10 km), it is clear that both earthquakes were near the northern limits of the Sawtooth fault. Dewey (1987) outlined a north-northeast-trending aftershock zone

that parallels the TCFS, but he did not relate these earthquakes to mapped faults in the area, in part, due to the sparse geologic mapping available at that time in this region.

Comparing geology with the earthquake catalog, we note that historic seismicity in the Stanley epicentral area has been concentrated along the northern portions of the Sawtooth fault and within Cretaceous rocks of the Idaho batholith (Fig. 3). In fact, the 1944, 1945, and 2020 sequences initiated to the north of the mapped Sawtooth fault trace (U.S. Geological Survey and Idaho Geological Survey, 2020). The mix of strike-slip and normal motions of the aftershocks near the intersection of the Sawtooth fault and the TCFS is consistent with local transtension (Fig. 2). This is similar to the 2014–2017 Challis earthquake sequence, where Pang *et al.* (2018) characterized the seismogenic behavior near the northern tip of the Lost River fault as normal slip along near-vertical conjugate shear zones or fault networks. Bruno *et al.* (2017) described similar strike-slip and oblique motion during the 1934 **M** 6.6 Hansel Valley earthquake, located at the end of a Basin and Range Province normal fault. Given the propensity for **M** 4.5+ earthquakes along the northern fault tips, the northern segments of both the Sawtooth and Lost River faults should be considered active, and fault databases should be updated to better represent the length and geometry of these complex faults.

Across the zone that is absent of any mapped normal faults between the Lost River and Sawtooth faults, Smith and Sbar (1974) and Dewey (1987) identified a zone of seismicity occurring from the 1960s through the 1980s that included six $\mathbf{M} > 4.5$ earthquakes (Fig. 1). Termed the White Cloud Peaks zone by Dewey (1987), Smith and Sbar (1974) suggested a normal fault dipping 46° to the east as the source of the 1963 **M** 4.9 earthquake, which occurred in this zone. The Lost River, Lemhi, and Beaverhead faults are all separated by a distance of 30–40 km. Because of the distance from the Lost River fault, Dewey (1987) speculated that the White Cloud Peaks zone corresponded to a developing first-order north- to northwest-trending fault similar to the adjacent faults. Link and Janecke (1999) identified both reverse and normal northwest-striking faults within this region that may support this claim. Although, there is no geomorphic or geologic evidence for recent fault activity, the historic patterns of seismicity space faults about every 30 km within the CTB (Fig. 1).

The deadliest and most notable earthquake in central Idaho is the 28 October 1983 M_w 6.9 Borah Peak earthquake (Fig. 1). This two-segment, 36 km long rupture was one of the largest historical intraplate normal-faulting earthquakes ever recorded. The earthquake resulted in the deaths of two young children and $12.5 million in damage (Stein and Bucknam, 1985; Bucknam and Stein, 1987). The earthquake initiated along a central segment of the Lost River fault at a depth of about 16 km and propagated northward across a segment boundary (e.g., Crone *et al.*, 1987; Haller and Crone, 2004; DuRoss *et al.*, 2019). Unlike the Stanley earthquake that produced no surface rupture, this is an example of a multisegment rupture, with a surface scarp that preserves the earthquake's slip.

On 13 April 2014, an M_w 4.8 earthquake struck the Challis, Idaho, area (Fig. 1). This earthquake and aftershock sequence were focused on an area, approximately, 25–30 km northwest of the 1983 M_w 6.9 Borah Peak earthquake epicenter along the northern Challis segment of the Lost River fault. Approximately, seven months later, on 3 January 2015, an M_L 5.0 earthquake occurred near the town of Challis (Fig. 1); this sequence continued into 2017. In total, about 1000 earthquakes were detected and located for this sequence (Pang *et al.*, 2018). These earthquakes clustered around four locations, mostly with strikes similar to the 1983 Borah Peak sequence. The steep northeast-dipping fault planes outlined by the Challis aftershocks differs from the 1983 Borah Peak aftershock sequence in that aftershock hypocenters aligned along moderate southwest dips that presumably outline the Lost River fault (Doser and Smith, 1985). Pang *et al.* (2018) concluded that all of the Challis events may be considered aftershocks of the 1983 earthquake sequence, where a third Lost River fault segment was activated (Fig. 1). In fact, based on recurrence of large earthquakes and estimated stress changes from the Borah Peak earthquake, they suggested that aftershocks will persist for 94 yr and possibly longer.

Fault Orientations and Terminations

Gravity and magnetic data together with the regional geology highlight patterns that may relate to fault segment boundaries and seismicity patterns within the CTB and TCFS regions (Fig. 3). For our analysis, we use the gravity and magnetic compilations of Mankinen *et al.* (2004). We show the complete Bouguer gravity anomaly and total magnetic field maps for central Idaho, with an emphasis on the Sawtooth and Lost River faults. We present a high-pass-filtered version of the gravity data, to suppress spatial wavelengths that exceed 100 km and highlight small scale upper crustal structures. We show the total-field magnetic data that highlight shallow magnetic rock distributions, and we present magnetic potential or pseudogravity data that attenuates shallow magnetic signals and reduces the data to the magnetic pole (e.g., Blakely, 1995). This process highlights upper crustal structure, highlights lineations that may define regionally significant structures, and allows for a direct comparison with the filtered gravity data. We compare gravity and magnetic data with mapped fault traces and segment boundaries identified through topographic or geomorphic signatures.

Gravity data

In contrast with the southern portions of the complete Bouguer gravity anomaly map that highlights the high-density mid- to lower-crustal mafic sill intrusions of the SRP (Fig. 3c; Mabey,

1976; Shervais and Hanan, 2008; DeNosaquo *et al.*, 2009), the high-pass-filtered gravity map highlights a regional gravity low within our study area (Fig. 3d). The southwest boundary of this low-gravity zone parallels 50 km of the Sawtooth fault, essentially the mapped fault trace length to the south of the Stanley earthquake aftershock region. This lineament is consistent with a transition from relatively high-density Idaho batholith rocks to the west of the fault to a region that contains mostly lower density Challis volcanic rocks, and Precambrian and Paleozoic sedimentary and metamorphic Basin and Range rocks to the east of the fault. Although, the related lineation roughly defines the eastern extent of the batholith, the Stanley aftershocks that lie to the north of the mapped Sawtooth fault do not follow this presumed structural boundary. Instead, the epicentral region encompasses a region that contains both Idaho batholith and Challis volcanic rocks (Fig. 3b). The lack of a density contrast across the northern epicentral area, coupled with little geologic evidence for dip-slip motion, suggest that either the unmapped northern portion of the Sawtooth fault has recorded a different slip history when compared with the mapped Sawtooth fault to the south, or that the 2020 earthquake sequence recorded motion along an unmapped fault with no surface expression. This suggests that either the northern Sawtooth fault region has only recently activated, or that a long-term kinematic change in fault behavior has been driven by an interaction with the TCFS and related rocks.

The filtered gravity map indicates that, although, low-density rocks occupy the hanging-wall side of the Sawtooth fault, this gravity low also outlines the southwestern limits of the northeast-trending Custer graben (Fig. 3d). Along the Sawtooth fault, the <10 mGal low extends from the southern limits of the fault, north to the southern limits of the 2020 aftershock region. Using the approach of Saltus and Jachens (1995), Mankinen *et al.* (2004) suggested that the basin within the Sawtooth Valley was only a few hundred meters of depth. This suggests that the total vertical relief across the Sawtooth fault is about 1.5 km, or consistent, with the maximum 0.2 mm/yr Quaternary vertical slip rate documented along the Sawtooth fault (Crone *et al.*, 2010). If a strong strike-slip component is consistent with previous earthquake sequences, this vertical slip rate may underestimate the long-term hazard or recurrence interval for this fault.

The filtered gravity map also highlights a few other key observations related to Basin and Range extension. The northeast-trending gravity low defines the northern limits of the 2014–2017 Challis epicentral region, perhaps providing structural control from the related Custer graben that extends to the northern segment boundary of the Lost River fault (Figs. 1 and 3). A hanging-wall gravity high (Willow Creek Hills) defines the boundary between the two segments that activated in 1983. DuRoss *et al.* (2019) suggested that this segment boundary modulates rather than impedes fault ruptures, supporting the observation that large earthquakes can cross structurally controlled segment boundaries. Indeed, if the gravity, geomorphic, and earthquake aftershock data define a northern Sawtooth fault segment near the town of Stanley, and if the scarp-producing ruptures documented by Thackray *et al.* (2013) require a rupture that is longer than just the central segment, this would support multisegment ruptures along the Sawtooth fault. However, the lack of earthquake timing and spatial extent of past ruptures along this fault limit our supposition.

Near the 1983 M_w 6.9 Borah Peak earthquake, Mankinen *et al.* (2004) modeled the ~20 mGal anomaly as a basin less than 1 km deep. There is no observable gravity low associated with the Lost River fault segments farther north, suggesting that either the top of range to the valley floor reflects a lower long-term slip rate when compared with the central fault segments, or a component of unrecorded strike-slip motion on these northern fault segments accommodates long-term fault motion. The relatively shallow basins that lie along the Sawtooth fault and Lost River fault contrast with the deep Pahsimeroi and Lemhi basins that lie adjacent to the Lemhi and Beaverhead faults, respectively. Although the northern segments of these two faults have produced essentially no recorded seismicity, the late Quaternary slip record must account for basin subsidence. This reinforces the high hazard nature of these faults and may point to different processes that drive extension along the northern portions of the Lemhi and Beaverhead faults.

Magnetic data

The northern limit of the Sawtooth fault corresponds to a change in rock magnetic properties (Fig. 3). Here, faults related to the TCFS define the northwestern limit to the magnetic high, where the northern aftershocks related to the Stanley earthquake rotates to a more northerly trend (N10°W). This supports the idea that existing geologic structures may be a controlling factor in the spatial aftershock patterns.

Along the central portion of the Sawtooth fault footwall, Lewis *et al.* (2012) mapped an ~20 km^2 Challis volcanic rock intrusive body that forms a prominent magnetic high (Fig. 3b, e). Though the northern boundary of the intrusion shows a diffuse magnetic signal, the southern mapped extent corresponds with a sharp northeast-trending magnetic lineament that is coincident with the inferred Sawtooth fault segment boundary of Thackray *et al.* (2013). They defined this segment boundary, based on a change in the fault scarp expression, in which few exposures could be identified to the south. To the south, the trend of the Sawtooth fault rotates about 20° to about N40°W. Although the magnetic lineation does not extend across the fault to the east, the White Cloud Peak seismic zone and northeast-trending faults are mapped in this area (Fig. 3a). Whether the White Cloud Peak zone is responding to Basin and Range-style extension or to other processes is unclear from current geologic maps and the seismicity catalog.

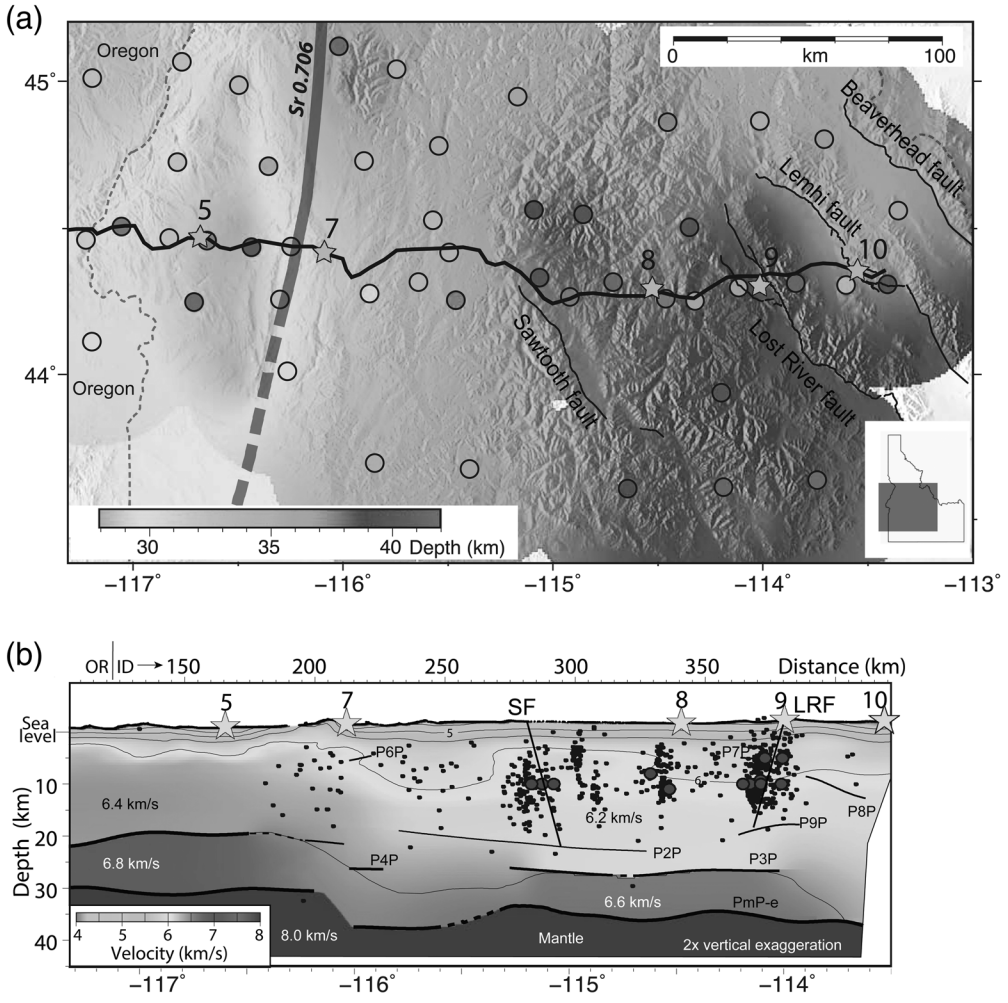

Figure 4. (a) Crustal thickness map constructed from receiver function inversions and a continuous spline interpolation (modified from Stanciu *et al.*, 2016). Each circle represents a station result. Black line represents the active seismic source receiver profile of Davenport *et al.* (2017). Stars represent explosive shot locations. Gray dashed and solid line represents the 0.706 isopleth that defines the transition from continental rocks to the east from accreted terrane rocks to the west. Major faults are labeled on the topographic map. Thin dashed lines represent the Idaho state border. Inset represents the mapped extent of (a) within the state of Idaho. (b) *P*-wave seismic tomogram and wide-angle reflection results from Davenport *et al.* (2017). We superimpose earthquake hypocenters between 44.1° and 44.5° N latitude (see Data and Resources) on the velocity model, with an inferred 60° east-dipping Sawtooth fault (SF) and a 60° west-dipping Lost River fault (LRF). Reflection labels are consistent with Davenport *et al.* 2017) interpretations.

Regardless, the convergence of a magnetic lineation that defines an abrupt geologic boundary, coupled with a change in fault trend and a zone of aligned and moderate seismicity, is consistent with a southern Sawtooth fault segment boundary, as defined by Thackray *et al.* (2013).

High susceptibility rocks occupy the region to the west of the Lost River fault north of Borah Peak (Fig. 3f). Seismicity related to the 1983 Borah Peak earthquake is essentially bound between the related N40°W magnetic lineation and the mapped trace of the Lost River fault. Though we do not explore this relationship here, we note that this magnetic high region has been identified as part of the Paleoproterozoic (1.6–2.4 Ga) Selway terrane that lies adjacent to the Grouse Creek Archean terrane (Foster *et al.*, 2006). These rocks and the related terrane boundary are not mapped in detail, but the correlation between spatial patterns of historic seismicity and ancient structures suggests that the CTB tectonics are influenced by relic geologic structures.

Central Idaho Fault Geometries

The Sawtooth fault mostly separates Paleozoic and older sedimentary rocks to the east from Cretaceous and younger intrusive rocks to the west (Fig. 3). Teleseismic receiver function data across the Sawtooth fault highlight this transition. Stanciu *et al.* (2016) explored the transition from accreted terranes that currently lie mostly within Oregon, across the paleocontinental margin, to the Lemhi and Beaverhead faults of eastern Idaho (Fig. 4a). Although the station contributions are relatively sparse for central Idaho, they show a clear thinning of the crust to the west of the Sawtooth fault and to the east of the Lemhi fault. Stanciu *et al.* (2016) attributed these crustal thickness changes to Precambrian sutures. Here, we suggest that these paleostructures may control active fault locations within the CTB of Idaho's Basin and Range.

The crustal thickness estimate of Stanciu *et al.* (2016) suggests a down-to-the east step across the Sawtooth fault and down-to-the west step across Lost River or Lemhi faults, or a region of thicker crust between extensional faults. Based on wide-angle active source seismic data, Davenport *et al.* (2017) supported this observation and identified prominent mid-crustal reflectors and mid-crustal velocities between the Sawtooth and Lost River faults that contained slower *P*-wave velocities (~6.2 km/s) than the surrounding region (Fig. 4b).

Although, both lateral and vertical resolution is limited with the receiver function and active source data, the observation of a thicker crust between the two active normal faults is atypical of Basin and Range extension and crustal thinning models (e.g., Hamilton, 1987). When we superimpose the hypocenter locations of earthquakes since 1940 on the Davenport *et al.* (2017) velocity cross section (hypocenters from ±0.2° latitude of the cross section), we observe a reasonable fit for a 60° or steeper east-dipping Sawtooth fault and a 60° west-dipping Lost River fault that lie within the crustal low-velocity region when compared with the neighboring areas (Fig. 4b). In addition, we observe the alignment of seismicity related to the White Cloud Peak zone identified by Dewey (1987) that is consistent with a more steeply dipping fault that lies between the Sawtooth and Lost River faults. We note that we removed catalog events for $\mathbf{M} < 4.5$ that were identified at the default depth of 10 km. We also note that the dip on the Lost River fault that we fit is steeper than the inferred 45°–53° west dip of Doser and Smith (1985), and that the 2020 aftershocks do not align to form an east-dipping fault. Regardless of these details, this seismicity pattern points to a broad region of extension that may kinematically link these two faults. Although, we cannot show a direct temporal link between these faults, we note the location of almost all large ($\mathbf{M} > 4.5$) central Idaho earthquakes lie between or along the northern portions of the Sawtooth and Lost River faults.

We observe that the maximum earthquake depth between the Sawtooth and Lost River faults corresponds with mid-crustal reflectors (P2P and P9P) identified from the wide-angle measurements (Davenport *et al.*, 2017; Fig. 4b). These reflectors likely represent the transition from brittle to ductile deformation at about 20 km depth. Although no surface expressions for the presumed faults outlined by the White Cloud Peak seismic zone have been documented, seismicity suggests that the region between the east-dipping Sawtooth and west-dipping Lost River faults is accommodating a zone of active extension.

Early Characteristics of Stanley Aftershocks

We examined the aftershock distribution of the Stanley earthquake over four months from 31 March 2020 through 31 July 2020 or 122 days, since the M_w 6.5 mainshock, to explore fault processes, damage potential from large aftershocks, and expected aftershock duration (Fig. 5). We compare this aftershock sequence to the 77 days that followed the 15 May 2020 M_w 6.5 Monte Cristo, Nevada, aftershock sequence and the 1983 through early 2020 M_w 6.9 Borah Peak aftershock sequence. We included aftershocks within a 50 km epicentral distance from the mainshock of the Stanley and Monte Cristo earthquakes, and we included the 70 km length of aftershocks highlighted by Pang *et al.* (2018) for the Borah Peak sequence. This broader zone that incorporates the Borah Peak region outlines the three northern Lost River fault segments that have documented motion between 1983 and 2017 (Pang *et al.*, 2018; DuRoss *et al.*, 2019).

For the Stanley earthquake, we observe a regular and consistent magnitude–frequency aftershock distribution. We estimate a b-value of 1.15 ($R^2 = 0.9963$) for cumulative aftershocks of greater than or equal to **M** 2.4 (Fig. 5a). We identify this completion magnitude, based on the expectation of increasing earthquake frequency with decreasing magnitude (Gutenberg and Richter, 1954). The high aftershock correlation coefficient above the completion magnitude suggests that the aftershocks have mostly remained within the northern Sawtooth fault segment, as defined by Thackray *et al.* (2013), with little spill over to adjacent faults. Because of the sparse network for near-real-time aftershock analysis, M_L was not calculated for many events $\mathbf{M} > 3.5$ (Fig. 5b). For this preliminary aftershock analysis, we assume that all of the M_w-derived magnitudes are equivalent to M_L earthquake magnitudes (e.g., Deichmann, 2017).

Figure 5c shows the exponential aftershock decay with time for $\mathbf{M} \geq 2.5$ Stanley aftershocks. Using the early aftershocks as a predictor of future seismicity, we use the modified Omori decay model (Utsu, 1961) to estimate earthquake occurrences (N) for 1 yr through 30 March 2021. Although, we show about 800 $\mathbf{M} \geq 2.5$ since 31 July 2020, the Omori decay curve predicts another ~350 aftershocks through the first year. Interestingly, the best fit to the Stanley aftershock sequence matches the exponent ($P = 0.75$) that Pang *et al.* (2018) estimated for the Borah Peak sequence (Fig. 5c). This low P-value may be related to the low heat flow values inferred at seismogenic depths within the Precambrian rocks of central Idaho (e.g., Brott *et al.*, 1981; Kisslinger and Jones, 1991; Foster *et al.*, 2006) or may suggest other aftershock characteristics that link the two earthquakes and fault systems.

To assess potential ground shaking from earthquake aftershocks, we explore a few models and relationships. First, we use Båth's law that states the maximum aftershock magnitude ($M_{a\,\max}$) is typically about **M** 1.2 less than the mainshock (Båth, 1965). This forecasts $M_{a\,\max}$ 5.3 for the largest Stanley aftershock. Shcherbakov and Turcotte (2004) revised the $M_{a\,\max}$ estimate based on the Gutenberg–Richter (G-R) scaling relationships shown in Figure 5a. They suggested that $M_{a\,\max}$ can be estimated by a/b in which a is the logarithm of the number of earthquakes with $\mathbf{M} > 0$ and b is the best-fit b-value slope, or in which the b-value slope reaches $N = 1$ for the aftershock sequence (Fig. 5a). For the Stanley sequence, the Shcherbakov approach predicts $M_{a\,\max}$ 5.0. To date, the largest recorded aftershock is an M_w 4.8 event that occurred on 1 April 2020. We recognize that the mixing of M_L and M_w events, and limited near-field seismic recordings, may influence this assessment.

Although, there are many aftershock forecast models, we highlight the Shcherbakov *et al.* (2004) approach, which introduces a frequency–magnitude relationship based on Båth's law

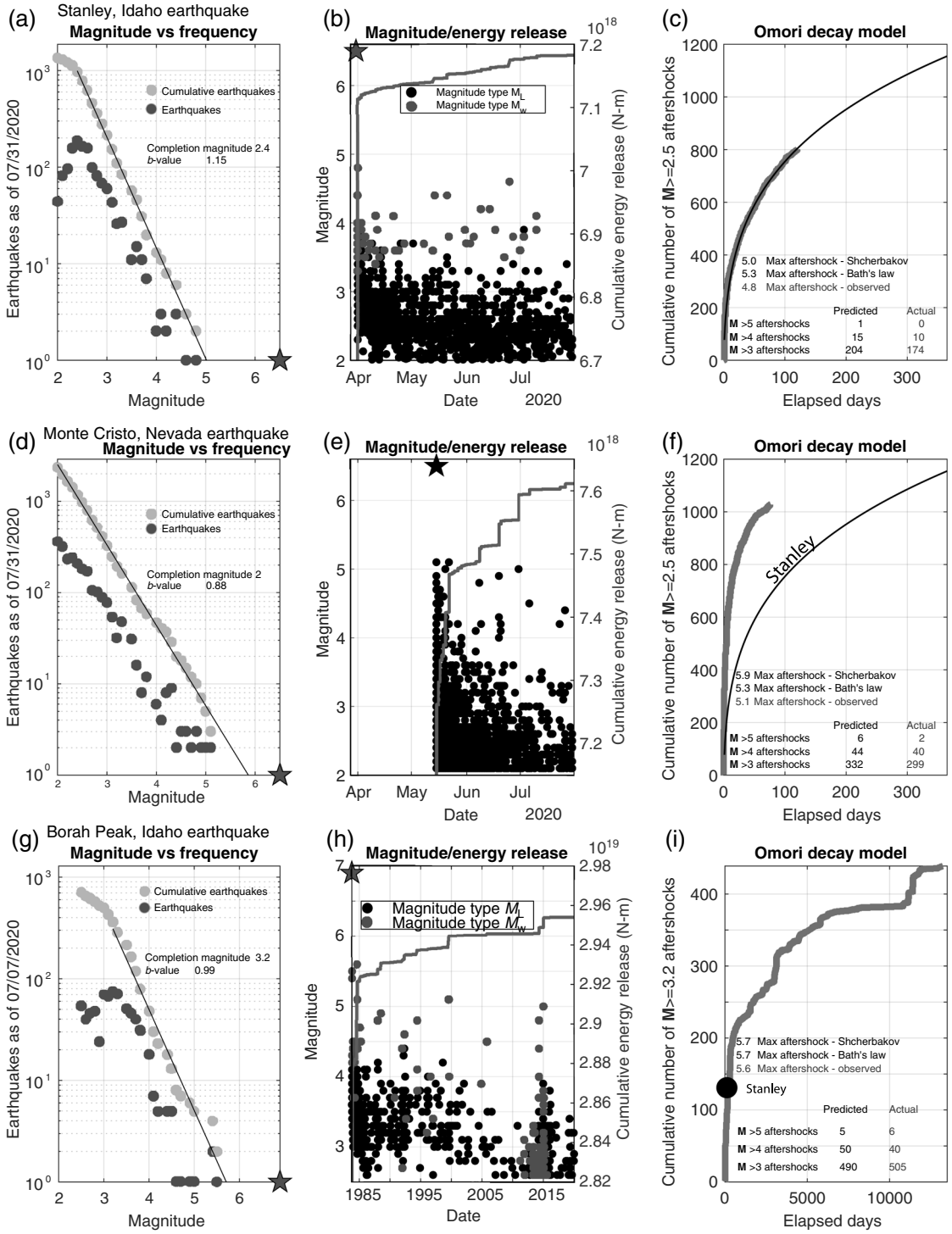

Figure 5. (a,d) Earthquakes versus magnitude for the Stanley and Monte Cristo earthquakes, respectively, from 31 March through 31 July 2020. (g) Earthquakes versus magnitude for the Borah Peak earthquake ranges from 1983 through 30 March 2020. Cumulative number of earthquakes that follow Gutenberg–Richter relationships are also shown on (a,d,g). (b,e,h) earthquake magnitude and cumulative energy release for the window through 31 July 2020 for the Stanley and Monte Cristo earthquakes, coded by magnitude type identified in the USGS catalog. The Borah Peak analysis covers a 37 yr window. (c,f,i) Cumulative number of **M** ≥ 2.5 earthquakes through 31 July for the Stanley and Monte Cristo earthquakes and for **M** ≥ 3.2 for a 37 yr window following the Borah Peak earthquake. The Stanley Omori decay model (thin line in (c,f)) predicts aftershock numbers through 31 March 2021 for the Stanley earthquake. Gray lines show observed aftershock numbers. Predictive aftershock numbers and magnitudes from Shcherbakov and Båth models are shown for each earthquake. Note that the total number of **M** ≥ 3.2 earthquakes related to the Stanley earthquake (circle on (i)) is similar to those recorded in the first four months of the Borah Peak earthquake.

and a modified G–R relationship. Here, the number of aftershocks (N_m) that exceeds a given magnitude (m) can be estimated by

$$N_m = 10^{b(M_{ms} - M_{a\max} - m)}, \quad (1)$$

in which M_{ms} represents the magnitude of the mainshock. To date for the Stanley earthquake, the Shcherbakov approach would predict $N_m = 1$ for $\mathbf{M} > 5$ aftershocks, $N_m = 15$ for $\mathbf{M} > 4$ aftershocks, and $N_m = 204$ for $\mathbf{M} > 3$ aftershocks. Figure 5 summarizes the four-month observed and predicted values of N, in which according to the Shcherbakov model, about 85% of the $\mathbf{M} > 3$ and about 67% of the $\mathbf{M} > 4$ earthquakes have already occurred for this sequence. This assumes that the Stanley earthquake remains a single segment rupture with a predictable aftershock sequence.

We perform the same analysis on the 15 May 2020 M_w 6.5 Monte Cristo, Nevada, earthquake that experienced a similar energy release and spatial aftershock distribution compared with the Stanley earthquake. Given the large number of $\mathbf{M} > 4$ earthquakes of the Monte Cristo sequence relative to Stanley aftershocks, we estimate a b-value of 0.88 ($R^2 = 0.9911$) through 31 July 2020, with about a 5% greater cumulative energy release compared with the Stanley earthquake for the first month after each mainshock (Fig. 5b,e). Because a more robust local seismic network is in place in western Nevada and eastern California, all earthquake magnitudes are provided as M_L, and the completion magnitude for this aftershock sequence is less than M_L 2 (Fig. 5d). However, for our analysis, we compare the aftershock decay model for $\mathbf{M} \geq 2.5$, as we did for the Stanley aftershock sequence. Using Båth's law, $M_{a\max}$ 5.3 is the same as the Stanley earthquake. However, because of a lower b-value compared with the Stanley earthquake, the Shcherbakov approach predicts $M_{a\max}$ 5.9. To date, the largest recorded aftershock for the Monte Cristo earthquake has been a pair of M_L 5.1 events (M_w 4.95 and 4.88, respectively).

The Shcherbakov relationship predicts $N_m = 6$ for $M_a > 5$, $N_m = 44$ for $M_a > 4$, and $N_m = 332$ for $M_a > 3$ for the Monte Cristo earthquake (Fig. 5). When we compare the Omori decay models of the two earthquakes, we observe a much more accelerated aftershock sequence related to the Monte Cristo earthquake (Fig. 5f). Through 31 July 2020, according to the Shcherbakov model, about 90% of the $M_a > 3$ and $M_a > 4$ aftershocks have occurred. This suggests that although the Monte Cristo earthquake initiated 45 days after the Stanley earthquake, its aftershock sequence is more advanced compared with the Stanley sequence. Here, we do not compare characteristics between the two fault systems, but a larger exponent of decay (P-value close to unity) better fits the Monte Cristo aftershock sequence. This may result from elevated thermal rock properties at seismogenic depths for western Nevada (Kisslinger and Jones, 1991; Coolbaugh *et al.*, 2005), when compared with central Idaho.

We next compare the Stanley aftershock sequence with the 1983 M_w 6.9 Borah Peak earthquake and aftershock sequence where we estimate a b-value of 0.99 ($R^2 = 0.9911$). Here, we use a completion magnitude of $\mathbf{M}$ 3.2 due to the sparse recording network over the past 37 yr (Fig. 5g). We include earthquakes from the mainshock through 30 March 2020 (Fig. 5h). We chose this end date as to not include any Stanley earthquakes in this analysis. For this sequence, both Båth's law and Shcherbakov's model predict $M_{a\max}$ 5.7, with an observed $M_{a\max}$ 5.6. The Shcherbakov model predicts $N = 6$ for $M_a > 5$, $N = 50$ for $M_a > 4$, and $N = 490$ for $M_a > 3$ (Fig. 5). For $M_a > 3$, we measure a completion ratio of 103.1%. This overestimate may be due, in part, to the inclusion of the 2014–2017 Challis earthquake sequence, which has been suggested as an aftershock of the Borah Peak sequence (Pang *et al.*, 2018). We note that $N = 131$ for $\mathbf{M} \geq 3.2$ aftershocks related to the Stanley earthquake at 122 days after the mainshock, which is greater than the observed $N = 99$ Borah Peak aftershocks $\mathbf{M} \geq 3.2$ for the same number of days (Fig. 3i). This may be related to an incomplete aftershock sequence in the first few weeks following the Borah Peak earthquake due to the sparse regional seismic network.

The similarity between decay curves of the Borah Peak and Stanley earthquakes may further support a kinematic link between the two fault systems. Pang *et al.* (2018) showed that the decay is independent of whether the Challis earthquakes are included in this analysis. This relationship and the spatial pattern of seismicity between the northeast-dipping Sawtooth fault, the southwest-dipping Lost River fault, and the presumed steeply dipping faults that lie between (Fig. 4b) warrants further investigations that explore a linkage of the active faults of central Idaho.

Temporary Seismic Monitoring Network

About 1 hr after the M_w 6.5 earthquake, we installed two Nanometrics Meridian Compact Posthole (MCPH) 120 s direct burial instruments in the granitic foothills of Boise, approximately, 100 km from the epicenter (Fig. 1). These instruments recorded two $\mathbf{M} > 4$ aftershocks, and numerous $\mathbf{M} > 3$ earthquakes. The following day (1 April 2020), two Boise State teams deployed six MCPH instruments within the epicentral region (Fig. 6). In addition, we installed two infrasound arrays to record audible earthquake-related signals, including avalanches, landslides, and aftershocks that may have coupled with the Earth's atmosphere. Two teams were required to deploy the instruments, because Idaho State Highway 21, near the earthquake epicenter, was closed to through traffic due to recent snowfall and avalanches that crossed the road. On 4–5 April 2020, we installed Z-land 3C Fairfield Nodal sensors (i.e., 5 Hz geophones) and additional broadband (120 s) instruments. The broadband and nodal stations were installed via snowmobile to add stations

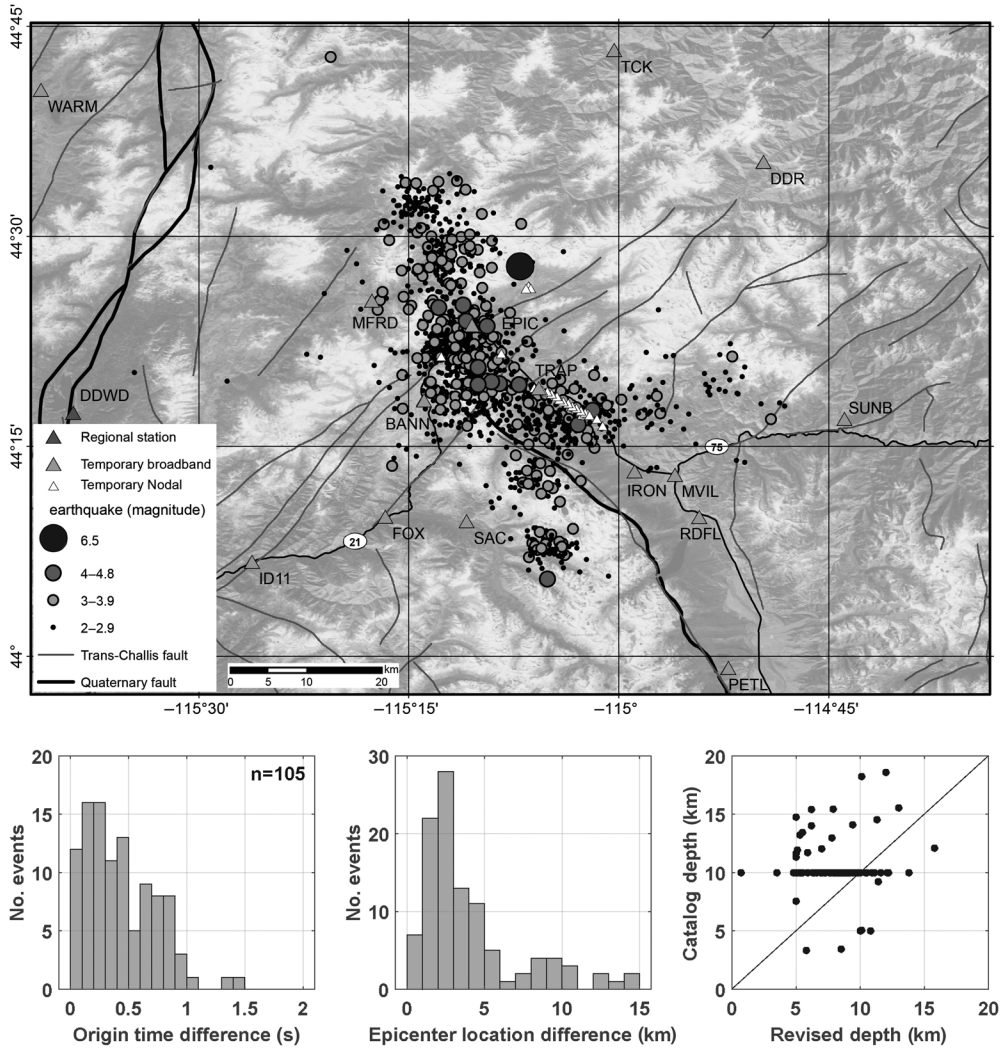

Figure 6. (Top) Aerial photograph overlain by the Stanley aftershock sequence. Temporary station locations and codes are also shown. Quaternary-active faults are from the Quaternary Fold and Fault Database (U.S. Geological Survey and Idaho Geological Survey, 2020), and northeast-striking faults of the TCFS are from Lewis *et al.* (2012). (Bottom) Preliminary assessment of the temporary deployment. We show time differences between 105 **M** > 3 earthquakes, and the epicentral location and depth differences between the catalog and temporary networks for these events.

close to the mainshock location. Many deployments required snow pits of greater than 1.5 m to reach soil. Two additional telemetered stations were installed in Stanley (MVIL) and Lowman, Idaho (ID11), for real-time monitoring (Fig. 6). Within one week of the mainshock, we installed, in total, 15 broadband sensors and 24 nodal sensors. With the addition of the 15 broadband stations that we deployed to the epicentral area after the mainshock, we expect that the catalog, during the operational time period, will be complete down to about **M** > 1. The temporary array was operational from April 2020 and will continue through the end of 2020.

While preliminary, we show differences between the earthquake catalog highlighted with earlier figures and early results from our temporary network. Based on analysis of 105 **M** > 3 aftershocks, we show a measurable earthquake time difference that results in epicentral locations that shift by as much as 15 km distance (Fig. 6). We also show that the catalog depth generally overestimates earthquake depths. With an improved velocity model that we will extract from the temporary network, we anticipate improved earthquake locations and moment tensor solutions. Continued monitoring, relocation of aftershocks, and moment tensor solutions based on the 15-station network will enable a more accurate assessment of the faults related to the Stanley sequence.

Conclusions

The 2020 M_w 6.5 Stanley earthquake initiated along the northern limits of the Sawtooth fault in central Idaho. Although, this fault has been known to support large, surface-rupturing earthquakes in the late Quaternary and Holocene, no surface rupture has been associated with this event. The 50 km long aftershock sequence outlines a N20° W trend that defines the northern mapped limits of the Sawtooth fault, a N10° W trend that extends farther to the north, and a third northeast-trending band of seismicity (Fig. 6). The northern aftershock region hosted the mainshock and intersects the northeast-trending TCFS that supported Eocene extension. The changing fault trend and northern termination of the Sawtooth normal fault is consistent with both the strike-slip and dip-slip motion observed during this earthquake sequence. From our preliminary analysis, we show that aftershocks have mostly remained within the footwall of the Sawtooth fault, along a steep, west-dipping trend. Geological and geophysical data reveal characteristics that define both the northern and southern fault limits and segment boundaries of both the Sawtooth and Lost River faults. Many of these active fault structures are collocated with

relic crustal structures, suggesting reactivation or, at least, some influence of older structures on the current tectonic environment. While not as great as the Monte Cristo, Nevada, earthquake sequence, the Stanley earthquake aftershocks provide regular energy release that is consistent with a low heat flow region of the crust at seismogenic depths. Historic patterns of seismicity suggest a kinematic link between the Sawtooth and Lost River faults.

We suggest that, to date, the active faults of central Idaho are poorly understood, and more work is needed to fully understand fault kinematics. The Stanley earthquake illustrates that potentially damaging earthquakes can occur away from mapped active faults, and, as with this earthquake, can leave little or no evidence in the geologic record. From this earthquake, we anticipate a renewed interest in the seismotectonics of central Idaho, and we anticipate advancing our understanding of this earthquake sequence through continued aftershock monitoring and analysis.

Data and Resources

The moment tensors described here are accessible from the Saint Louis University Earthquake Center available at http://www.eas.slu.edu/eqc/ (last accessed July 2020), the Global Centroid Moment Tensor (CMT) catalog search at https://www.globalcmt.org/CMTsearch.html (last accessed July 2020), and the National Earthquake Information Center (NEIC) at https://earthquake.usgs.gov (last accessed July 2020). Gravity and magnetic data are from Mankinen *et al.* (2004). All seismic data from the temporary network are archived at Incorporated Research Institutions for Seismology (IRIS) – network code XP. Other relevant data are from https://earthquake.usgs.gov/earthquakes (last accessed May 2020).

Acknowledgments

Earthquake source parameters used, including phase arrival-time data, are available in the U.S. Geological Survey Comprehensive Catalog of Earthquakes (http://earthquake.usgs.gov/earthquakes/map/). Derrick Chambers from the National Institute for Occupational Safety and Health (NIOSH) graciously provided 24 nodal sensors. Incorporated Research Institutions for Seismology–Program for the Array Seismic Studies of the Continental Lithosphere (IRIS/PASSCAL) provided six 40 s Trillium Compact Posthole broadband sensors. Assistance and support from Emily Wolin at the U.S. Geological Survey and Claudio Berti from the Idaho Geological Survey are greatly appreciated, as are discussions with Suzette Payne and Bertrand Delouis. The authors thank Jeffery Johnson, Thomas Otheim, and Jacob Anderson from Boise State University for their help in the rapid deployment of the temporary seismic network in the days following the mainshock. Funding was provided by the U.S. Geological Survey (Award G20AP00076), Battelle Energy Alliance (Award 3638008), and National Science Foundation (Award 2029940). Improvements in this article were provided by Chris DuRoss and an anonymous reviewer.

References

Anders, M. H., J. W. Geissman, L. A. Piety, and J. T. Sullivan (1989). Parabolic distribution of circum eastern Snake River Plain seismicity and latest Quaternary faulting: Migratory pattern and association with the Yellowstone hotspot, *J. Geophys. Res.* **94,** no. B2, 1589–1621.

Anders, M. H., D. W. Rodgers, S. R. Hemming, J. Saltzman, V. J. DiVinere, J. T. Hagstrum, G. F. Embree, and R. C. Walter (2014). A fixed sublithospheric source for the late Neogene track of the Yellowstone hotspot: Implications of the Heise and Picabo Volcanic Fields, *J. Geophys. Res.* **119,** no. B010483, 2871–2906, doi: 10.1002/2013JB010483.

Båth, M. (1965). Lateral inhomogeneities in the upper mantle, *Tectonophysics* **2,** 483–514.

Bennett, E. H. (1986). Relationship of the trans-Challis fault system in central Idaho to Eocene and basin and range extensions, *Geology* **14,** no. 6, 481–484.

Blakely, R. J. (1995). *Potential Theory in Gravity and Magnetic Applications*, Cambridge University Press, New York, New York, 441 pp.

Breckenridge, R. M., R. S. Lewis, G. W. Adema, and D. W. Weisz (2003). Miocene and younger faults in Idaho, *Idaho Geol. Surv. Map 8*, Scale 1:1,000,000, 1 Sheet.

Brott, C. A., D. D. Blackwell, and J. P. Ziagos (1981). Thermal and tectonic implications of heat flow in the eastern Snake River Plain, Idaho, *J. Geophys. Res.* **86,** 11709–11734.

Bruno, P. P. G., C. B. DuRoss, and S. Kokkalas (2017). High-resolutions seismic profiling reveals faulting associated with the 1934 Ms 6.6 Hansel Valley earthquake (Utah, USA), *Geol. Soc. Am. Bull.* **129,** 1227–1240, doi: 10.1130/B31516.1.

Bucknam, R. C., and R. Stein (1987). Preface to collection of papers on the 1983 Borah Peak, Idaho, earthquake, *Bull. Seismol. Soc. Am.* **77,** 691–693.

Coolbaugh, M., R. Zehner, C. Kreemer, D. Blackwell, and G. Oppliger (2005). A map of geothermal potential for the Great Basin, USA: Recognition of multiple geothermal environments, *Geoth. Res. Council Trans.* **29,** 223–228.

Crone, A. J., and K. M. Haller (1991). Segmentation and the coseismic behavior of Basin and Range normal faults: Examples from east-central Idaho and southwestern Montana, USA, *J. Struct. Geol.* **13,** no. 2, 151–164.

Crone, A. J., K. M. Haller, and R. S. Lewis (Compilers) (2010). Fault number 640, Sawtooth fault, in Quaternary fault and fold database of the United States, U.S. Geological Survey website, available at https://earthquakes.usgs.gov/hazards/qfaults (last accessed May 2020).

Crone, A. J., M. N. Machette, M. G. Bonilla, J. J. Lienkaemper, K. L. Pierce, W. E. Scott, and R. C. Bucknam (1987). Surface faulting accompanying the Borah Peak earthquake and segmentation of the Lost River fault, central Idaho, *Bull. Seismol. Soc. Am.* **77,** no. 3, 739–770.

Davenport, K. K., J. A. Hole, B. Tikoff, R. M. Russo, and S. H. Harder (2017). A strong contrast in crustal architecture from accreted terranes to craton, constrained by controlled-source seismic data in Idaho and eastern Oregon, *Lithosphere* **9,** no. 2, 325–340.

Deichmann, N. (2017). Theoretical basis for the observed break in M_L/M_w scaling between small and large earthquakes, *Bull. Seismol. Soc. Am.* **107,** no. 2, 505–520.

DeNosaquo, K. R., R. B. Smith, and A. R. Lowry (2009). Density and lithospheric strength models of the Yellowstone–Snake River Plain

volcanic system from gravity and heat flow data, *J. Volcanol. Geoth. Res.* **188,** nos. 1/3, 108–127.

Dewey, J. W. (1987). Instrumental seismicity of central Idaho, *Bull. Seismol. Soc. Am.* **77,** no. 3, 819–836.

Doser, D. I., and R. B. Smith (1985). Source parameters of the 28 October 1983 Borah Peak, Idaho, earthquake from body wave analysis, *Bull. Seismol. Soc. Am.* **75,** no. 4, 1041–1051.

Doser, D. I., and R. B. Smith (1989). An assessment of source parameters of earthquakes in the Cordillera of the western United States, *Bull. Seismol. Soc. Am.* **79,** no. 5, 1383–1409.

DuRoss, C. B., M. P. Bunds, R. D. Gold, R. W. Briggs, N. G. Reitman, S. F. Personius, and N. A. Toké (2019). Variable normal-fault rupture behavior, northern Lost River fault zone, Idaho, USA, *Geosphere* **15,** no. 6, 1869–1892.

Dziewonski, A. M., T. A. Chou, and J. H. Woodhouse (1981). Determination of earthquake source parameters from waveform data for studies of global and regional seismicity, *J. Geophys. Res.* **86,** 2825–2852, doi: 10.1029/JB086iB04p02825.

Ekström, G., M. Nettles, and A. M. Dziewonski (2012). The global CMT project 2004-2010: Centroid-moment tensors for 13,017 earthquakes, *Phys. Earth Planet. In.* **200/201,** 1–9, doi: 10.1016/j.pepi.2012.04.002.

Fisher, F. S., D. H. Mclntyre, and K. M. Johnson (1983) *Geologic map of the Challis 1x2 degree quadrangle, Idaho, U.S. Geol. Surv. Open-File Rept. 83-523*, Scale 1:250,000.

Foster, D. A., P. A. Mueller, D. W. Mogk, J. L. Wooden, and J. J. Vogl (2006). Proterozoic evolution of the western margin of the Wyoming craton: Implications for the tectonic and magmatic evolution of the northern Rocky Mountains, *Can. J. Earth Sci.* 43**,** no. 10, 1601–1619.

Geomatrix Consultants, Inc. (1989). Final report seismotectonic evaluation for Little Wood River Dam site, *Tech. Rept. U.S. Dept. Int.*, Bureau of Reclamation, Denver, Colorado, 104 pp., 2 pls.

Gutenberg, B., and C. F. Richter (1954). *Seismicity of the Earth and Associated Phenomenon*, Second Ed., Princeton Univ. Press, Princeton, New Jersey.

Haller, K. M., and A. J. Crone (2004). Twenty years after the Borah Peak earthquake: Field guide to surface-faulting earthquakes along the Lost River fault, Idaho, in *Geological Field Trips in Southern Idaho, Eastern Oregon, and Northern Nevada*, K. M. Haller and S. H. Wood (Editors), *U.S. Geol. Surv. Open-File Rept. 2004-1222*, 118–135.

Haller, K. M., and R. L. Wheeler (Compilers) (2010). Fault number 601c, Lost River fault, Thousand Springs section, in Quaternary fault and fold database of the United States, U.S. Geological Survey website, available at https://earthquakes.usgs.gov/hazards/qfaults (last accessed May 2020).

Hamilton, W. (1987). Crustal extension in the basin and range province, southwestern United States, *Geol. Soc. Lond. Spec. Publ.* **28,** no. 1, 155–176.

Idaho Geological Survey (2020). Stanley Lake liquefaction page, available at https://www.idahogeology.org/stanley-lake-liquefaction (last accessed June 2020).

International Seismological Centre (2020). On-line Bulletin, doi: 10.31905/D808B830.

Kiilsgaard, T. H., F. S. Fisher, and E. H. Bennett (1986). The trans-Challis fault system and associated precious metal deposits, Idaho, *Econ. Geol.* **81,** no. 3, 721–724.

Kiilsgaard, T. H., V. L. Freeman, and J. S. Coffman (1970). Mineral resources of the Sawtooth primitive area, Idaho, in *Studies Related to Wilderness–Primitive Areas*, Geol. Surv. Bull. 1319-D, United States Government Printing Office, Washington.

Kisslinger, C., and L. M. Jones (1991). Properties of aftershock sequences in southern California, *J. Geophys. Res.* **96,** no. B7, 11,947–11,958.

Koper, K. D., K. L. Pankow, J. C. Pechmann, J. M. Hale, R. Burlacu, W. L. Yeck, H. M. Benz, R. B. Herrmann, D. T. Trugman, and P. M. Shearer (2018). Afterslip enhanced aftershock activity during the 2017 earthquake sequence near Sulphur Peak, Idaho, *Geophys. Res. Lett.* **45,** no. 11, 5352–5361.

Lewis, R. S., P. K. Link, L. R. Stanford, and S. P. Long (2012). Geologic map of Idaho, *Idaho Geol. Surv. Geol. Map 9*, Scale 1:750,000.

Link, P. K., and S. U. Janecke (1999). Geology of east-central Idaho: Geologic roadlogs for the Big and Little Lost River, Lemhi, and Salmon River Valleys, in *Guidebook to the Geology of Eastern Idaho: Pocatello*, S. S. Hughes and G. D. Thackray (Editors), Idaho Museum of Natural History, 295–334.

Mabey, D. R. (1976). Interpretation of a gravity profile across the western Snake River Plain, Idaho, *Geology* **4,** no. 1, 53–55.

Mankinen, E. A., T. G. Hildenbrand, M. L. Zientek, S. E. Box, A. A. Bookstrom, M. H. Carlson, and J. C. Larsen (2004). Guide to geophysical data for the northern Rocky Mountains and adjacent areas, Idaho, Montana, Washington, Oregon, and Wyoming, *U.S. Geol. Surv. Open-File Rept. 2004-1413*, 34 pp.

O'Neill, J. M., and D. A. Lopez (1985). Character and regional significance of the Great Falls tectonic zone, east-central Idaho and west-central Montana, *Am. Assoc. Petrol. Geol. Bull.* **69,** 437–447.

Pang, G., K. D. Koper, M. C. Stickney, J. C. Pechmann, R. Burlacu, K. L. Pankow, S. Payne, and H. M. Benz (2018). Seismicity in the Challis, Idaho, region, January 2014–May 2017: Late aftershocks of the 1983 M_s 7.3 Borah Peak earthquake, *Seismol. Res. Lett.* **89,** 1366–1378, doi: 10.1785/0220180058.

Payne, S. J., R. McCaffrey, R. W. King, and S. A. Kattenhorn (2012). A new interpretation of deformation rates in the Snake River Plain and adjacent basin and range regions based on GPS measurements, *Geophys. J. Int.* **189,** 101–122.

Pierce, K. L., and L. A. Morgan (1992). The track of the Yellowstone hot spot: Volcanism, faulting, and uplift, *Reg. Geol. E. Idaho West. Wyoming: Geol. Soc. Am. Memoir* **179,** no. 322, 1–53.

Pollitz, F. F., C. Wicks, W. L. Yeck, and J. Evans (2019). Fault slip associated with the 2 September 2017 M 5.3 Sulphur Peak, Idaho, earthquake and aftershock sequence, *Bull. Seismol. Soc. Am.* **109**, no. 3, 875–887.

Reid, R. R. (1963). *Reconnaissance Geology of the Sawtooth Range*, Idaho Bureau of Mines and Geology Pamphlet 129, 37 pp., 2 pls.

Rember, W. C., and E. H. Bennett (1979). Geologic map of the Hailey quadrangle, Idaho, Idaho Bureau of Mines and Geology, Geologic Map Series, Scale 1:250,000.

Richins, W. D., J. C. Pechmann, R. B. Smith, C. J. Langer, S. K. Goter, J. E. Zollweg, and J. J. King (1987). The 1983 Borah Peak, Idaho, earthquake and its aftershocks, *Bull. Seismol. Soc. Am.* **77,** no. 3, 694–723.

Rodgers, D. W., H. T. Ore, R. T. Bobo, N. McQuarrie, and N. Zentner (2002). Extension and subsidence of the eastern Snake River Plain, Idaho, in *Tectonic and Magmatic Evolution of the Snake River Plain Volcanic Province*, B. Bonnichsen, C. White, and M. McCurry (Editors), Idaho Geological Survey, *Bulletin 30*, 121–155.

Saltus, R. W., and R. C. Jachens (1995). Gravity and basin-depth maps of the Basin and Range Province, Western United States, *U.S. Geol. Surv. Map GP-1012*, scale 1:2,500,000.

Sandwell, D., R. Mellors, X. P. Tong, M. Wei, and P. Wessel (2011). Open radar interferometry software for mapping surface deformation, *Eos Trans. AGU* **92,** no. 28, 234–234.

Scott, W. E., K. L. Pierce, and M. H. Hait (1985). Quaternary tectonic setting of the 1983 Borah Peak earthquake, central Idaho, *Bull. Seismol. Soc. Am.* **75,** 1053–1066.

Shcherbakov, R., and D. L. Turcotte (2004). A modified form of Båth's law, *Bull. Seismol. Soc. Am.* **94,** no. 5, 1968–1975.

Shcherbakov, R., D. L. Turcotte, and J. B. Rundle (2004). A generalized Omori's law for earthquake aftershock decay, *Geophys. Res. Lett.* **31,** L11613, doi: 10.1029/2004GL019808.

Shervais, J. W., and B. B. Hanan (2008). Lithospheric topography, tilted plumes, and the track of the Snake River–Yellowstone hot spot, *Tectonics* **27,** no. 5, doi: 10.1029/2007TC002181.

Smith, R. B., and M. L. Sbar (1974). Contemporary tectonics and seismicity of the western United States with emphasis on the Intermountain Seismic Belt, *Geol. Soc. Am. Bull.* **85,** no. 8, 1205–1218.

Stanciu, C. A., R. M. Russo, V. I. Mocanu, P. M. Bremner, S. Hongsresawat, M. E. Torpey, J. C. VanDecar, D. A. Foster, and J. A. Hole (2016). Crustal structure beneath the Blue Mountains terranes and cratonic North America, eastern Oregon, and Idaho, from teleseismic receiver functions, *J. Geophys. Res.*, **121,** 5049–5067

Stein, R., and R. C. Bucknam (1985). Proceedings of the workshop XXVIII on the Borah Peak, Idaho, earthquake, *U.S. Geol. Surv. Open-File Rept. 85-290*, 685 pp.

Stickney, M. C., and M. J. Bartholomew (1987). Seismicity and Quaternary faulting of the northern Basin and Range province, Montana and Idaho, *Bull. Seismol. Soc. Am.* **77,** 1602–1625.

Thackray, G. D., D. W. Rodgers, and D. Streutker (2013). Holocene scarp on the Sawtooth fault, central Idaho, USA, documented through lidar topographic analysis, *Geology* **41,** no. 6, 639–642.

Tschanz, C. M., T. H. Kiilsgaard, and D. A. Seeland (1986). Geology of the eastern part of the Sawtooth National Recreation Area, Idaho, *U.S. Geol. Surv. Bull. 1545-A*, 17–43, 1 pl., Scale 1:62,500.

Umpleby, J. B., and D. C. Livingston (1920). A reconnaissance in south central Idaho embracing the Thunder Mountain, Big Creek, Stanley basin, Sheep Mountain, and Seafoam districts, *Idaho Bureau of Mines and Geology Bulletin 3*, 23 pp.

U.S. Geological Survey (2020a). M6.5 Stanley earthquake event page, available at https://earthquake.usgs.gov/earthquakes/eventpage/us70008jr5/executive (last accessed June 2020).

U.S. Geological Survey (2020b). Comprehensive earthquake catalog, available at https://earthquake.usgs.gov/earthquakes/search/ (last accessed August 2020).

U.S. Geological Survey and Idaho Geological Survey (2020). Quaternary fault and fold database for the United States, available at https://www.usgs.gov/natural-hazards/earthquake-hazards/faults (last accessed May 2020).

Utsu, T. (1961). A statistical study on the occurrence of aftershocks, *Geophys. Mag.* **30,** 521–605.

Wells, D. L., and K. J. Coppersmith (1994). New empirical relationships among magnitude, rupture length, rupture width, rupture area, and surface displacement, *Bull. Seismol. Soc. Am.* **84,** no. 4, 974–1002.

Wessel, P., and W. H. F. Smith (1998). New, improved version of Generic Mapping Tools released, *Eos Trans. AGU* **79,** no. 47, 579, doi: 10.1029/98EO00426.

Manuscript received 11 September 2020
Published online 9 December 2020